Electronic Structure of Interstitial Hydrogen in Lutetium Oxide from DFT+U calculations and Comparison Study with μSR Spectroscopy

E. Lora da Silva*
Department of Chemistry, University of Bath, Bath BA2 7AY, UK

A. G. Marinopoulos, R. B. L. Vieira, R. C. Vilão, H. V. Alberto, J. M. Gil
CFisUC, Department of Physics, University of Coimbra, P-3004-516 Coimbra, Portugal

R. L. Lichti, P. W. Mengyan, B. B. Baker
Department of Physics, Texas Tech University, Lubbock TX 79409-1051, USA
(Dated: May 12, 2016)

Abstract

The electronic structure of hydrogen impurity in Lu_2O_3 was studied by first-principles calculations and muonium spectroscopy. The computational scheme was based on two methods: first, a semi-local functional of conventional density-functional theory (DFT) and secondly a DFT+U approach which accounts for the on-site correlation of the $4f$ electrons via an effective Hubbard-type interaction. Three different types of stable configurations were found for hydrogen depending upon its charge state. In its negatively-charged and neutral states, hydrogen favors interstitial configurations residing either at the unoccupied sites of the oxygen sublattice or at the empty cube centers surrounded by the lanthanide ions. In contrast, the positively-charged state stabilized only as a bond configuration, where hydrogen binds to oxygen ions.

Overall, the results between the two methods agree in the ordering of the formation energies of the different impurity configurations, though within DFT+U the charge-transition (electrical) levels are found at Fermi-level positions with higher energies. Both methods predict that hydrogen is an amphoteric defect in Lu_2O_3 if the lowest-energy configurations are used to obtain the charge-transition, thermodynamic levels.

The calculations of hyperfine constants for the neutral interstitial configurations show a predominantly isotropic hyperfine interaction with two distinct values of 926 and 1061 MHz for the Fermi-contact term originating from the two corresponding interstitial positions of hydrogen in the lattice. These high values are consistent with the muonium spectroscopy measurements which also reveal a strongly isotropic hyperfine signature for the neutral muonium fraction with a magnitude slightly larger (1130 MHz) from the ab-initio results (after scaling with the magnetic moments of the respective nuclei).

PACS numbers: 71.55.Ht, 76.75.+i, 71.75.Mb, 71.15.Nc, 71.20.Ps

I. INTRODUCTION

Lanthanide sesquioxides of the M_2O_3 stoichiometry (M a trivalent lanthanide cation) have attracted considerable interest in many industrial applications in catalysis, solid-state lighting, oxygen and hydrogen storage and as permanent magnets.[1] These oxides are also promising in high-κ technology as potential gate materials in the next generation of field-effect transistors. They possess high dielectric constants (~ 30)[2] and can act as insulators with gap widths up to 6 eV,[2] enabling band offsets with respect to the adjoining semiconductor of over 1 eV, thus minimizing carrier injection into its bands by acting as potential barriers.[2,3] Lanthanide sesquioxides are also thermodynamically stable in contact with Si, inhibiting the formation of thin insulating layers at the interface.[2]

A good control of the oxide behavior in these diverse applications requires a fundamental understanding of the types of defects that can be created, either inside the oxide or at the interface with the surrounding vapour or other material components. Defects or dopants may appear in semiconductors and insulators at any stage of the system, from initial growth conditions to ageing of fully developed devices[2,4–6] affecting their properties and reliability. Hydrogen is an ubiquitous impurity, which can be unintentionally incorporated during the growth environment,[7] in particular in the presence of water for Lu_2O_3.[8] Hydrogen exhibits complex behaviour when introduced in semiconductors and dielectrics.[9,10] It can act as an amphoteric impurity interacting with other dopants present in the material, where it may counteract the electric conductivity by passivating these dopant sources; or it can enable a donor level close to the conduction band, thus inducing n-type conductivity.[7] When samples are exposed to source gases containing hydrogen (up to about 1000°C for all practically obtainable water-vapour levels), either in the form of interstitial protons or hydroxide ions,[11,12], it will dominate the ionic conductivity of the material at low temperatures.[11,12]

Very limited theoretical studies of the defect physics of lanthanide oxides have been performed to date.[6,13] The main reason is that, from a theoretical perspective, their electronic structure is quite challenging. These materials are mixed valence systems, characterized by the highly localized $4f$-electron states of the lanthanide that couple strongly with the *spd* states.[14,15] The strong electron-electron correlation within these f-electron shells is poorly described by local (LDA) or semi-local (GGA) functionals based on density-functional theory (DFT). Instead, these functionals, due to an incomplete cancellation of the Coulomb self-interaction, favour delocalization[15] for the (partially)-occupied f-

states, therefore resulting in an incorrect description of the insulating properties of the oxides.[14,16]

In principle, the self-interaction error and the inadequate description of correlations can be partly corrected by employing hybrid-functional approaches, where a portion of the Hartree-Fock exact exchange is included.[14] For magnetically-ordered phases, such hybrid functionals significantly improve the description of the electronic structure of d- and f-electron systems, when compared to direct and inverse photo-emission experiments.[14] This improvement is achieved by splitting the partially occupied d- and f-states into occupied and unoccupied manifolds.[14] Accurate electronic-structure studies of lanthanide/rare-earth sesquioxides and CeO_2 have also been carried out by employing hybrid functionals (HSE03 and HSE06), and the screened exchange LDA (sX-LDA).[16] It has been observed that these methods describe the strongly correlated f-electrons quite well, yielding the correct band-gaps and trends across the lanthanide series. sX-LDA also tends to predict the unoccupied $4f$ levels at higher energies, leading to a better agreement with experiments,[16] when compared to the G0W0@LDA+U results.[17]

However, the use of hybrid functionals in studies of defects is computationally demanding, especially when dealing with lanthanide systems where the $4f$ electrons are part of the valence-electron shells. Such use is also not exempt of errors when employed in conjunction with certain types of pseudopotentials, i.e. ultrasoft or norm-conserving pseudopotentials.[18]

For the present work, DFT calculations were carried out to study the hydrogen impurity in Lu_2O_3. Lu_2O_3 possesses a full $4f$-electron shell and due to the advantage of the spin-density being arranged in an antiferromagnetic ordering, at very low temperatures (below the Néel temperature),[14] it is therefore possible to rely on the adequacy of athermal DFT calculations to provide a reasonable description of the structural properties.

More specifically, we have used two different approaches. The first was to employ a semi-local (GGA) DFT functional with the localized $4f$-shell treated as a core-like shell. This method is usually referred to as the standard model or ionic model[19] and has been employed in the past for the study of lanthanide and rare-earth systems.[20] The main justification for this approach is that it avoids an important drawback of local (LDA) and semi-local (GGA) DFT functionals. By employing these functionals, without imposing the frozen-core approximation, the localization of the $4f$ states is predicted to be too weak, therefore, yielding a very strong hybridization with the other valence states and much too large density of states at the Fermi level. It is noteworthy of mentioning that the standard model does not account for all aspects of lanthanide-rare-earth electronic properties (such as magnetism) which need a more refined coupling of the f-states with the remaining valence states.[19] The second approach was based on a DFT+U methodology that accounts for the on-site $4f$-electron correlations via an effective Hubbard-type potential. The $4f$-electron shell was treated as being part of the valence shells and the magnitude of the effective Hubbard parameter was chosen to minimize the overlap between the $4f$ and sp-valence states. This approach is computationally as efficient as conventional DFT and, therefore, well suited for defect studies which require a large number of atoms and electrons.

Using theses approaches we determined the configurations and electronic structure of isolated hydrogen states in Lu_2O_3. The geometrical configurations of interstitial hydrogen were explored in detail for all possible charge states that hydrogen can assume. From the minimum-energy configurations, we further determined the electrical levels of hydrogen, the induced defect levels in the gap and resulting hyperfine constants.

Isolated hydrogen impurities are difficult to probe experimentally due to their high mobilities which favour pairing with other defects.[13,21,22] The use of microscopic techniques like electron paramagnetic resonance (EPR) or infrared (IR) vibrational spectroscopy in order to obtain microscopic information about hydrogen configurations and levels such as those calculated in this work is thus limited to a couple of systems where hydrogen is usually present in high concentrations.[23–26] However, this microscopic information about hydrogen configurations can be obtained by using muonium (the bound state of a positive muon with an electron) as a light pseudo-isotope of hydrogen.[27,28] Beams of positive muons are available in international muon spin research (μSR) installations and muonium spectroscopy has been successfully used in order to determine muonium (and therefore hydrogen) charge-transition levels and sites, often in a synergistic approach with ab-initio studies.[29–34] Moreover, muonium spectroscopy can provide detailed information about the electronic structure of muonium/hydrogen through the hyperfine interaction.[35–39] Such information is almost non-existent for isolated hydrogen from any other technique.[40]

Muon spin rotation measurements were completed on a polycrystalline sample of Lu_2O_3. During this experiment, magnetic fields up to 7 T were applied across the sample in a direction perpendicular (transverse) to the incoming muon spin polarization direction, at room temperature (300 K) and at 2.5 K. Data analyses were performed with the MSRFIT and WiMDA codes.[41]

The paper is thus organized as follows: Sec. II contains an explanation of the theoretical methodology adopted in the present work together with a description of the lattice of Lu_2O_3. The obtained results on hydrogen structural configurations, formation energies, local electronic states and hyperfine constants are presented in Sec. III. In the same section the μSR data and related analysis are also provided. Finally, our conclusions are presented in Sec. IV.

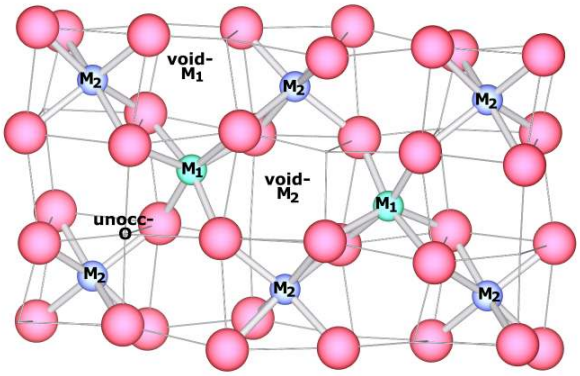

FIG. 1. (Color online) Part of the conventional cell of Lu_2O_3. O is represented by the larger red spheres and Lu by the smaller blue and green spheres, to distinguish between the two different metal sites, M_1 and M_2, respectively. The structural interstitial sites: voids and unoccupied sites of the lattice are labelled accordingly.

II. THEORETICAL METHOD

The primitive unit cell of Lu_2O_3 consists of a 40-atom body-centred cubic (BCC) structure,[42] corresponding to the space-group Ia3-(Th7) (N. 206), with a conventional cell that can be represented as an 80-atom cubic c-type structure (Fig. 1).[42,43] The structure is formed by 64 slightly distorted minicubes composed of O anions at the vertices. Only 32 centres of these minicubes are occupied by the Lu metal (M) cations, and the remaining are empty (denoted as structural void-M sites). The cations are positioned at two different crystallographic symmetry sites, with M_1 belonging to the 8b site and M_2 at the 24d site (Fig. 1). The anions are positioned at the 48e crystallographic sites. The eight vertices of the minicubes are occupied by six anions only, therefore enabling an octahedral coordination for the cations.[15,42] The unoccupied O vertices will be henceforth denoted as unocc-O sites. For the M_2-centred minicubes, three O ions are positioned at one face of the cube, and the other three are at the opposite face, all of the six anions being equally distanced from the cation center (2.24 Å). The vertices of the M_1-centred minicubes are formed by four O ions at one face and the other two at the opposite face - the distance between the anions and the respective cation center occurs with three different paired distances (2.30, 2.22, 2.20 Å).[44] Fig. 1 represents part of the conventional cell of luthetia denoted with the above mentioned crystallographic sites (created by using the visualization program VESTA[45]).

In the present theoretical study, two spin-polarized DFT approaches were employed: the generalized-gradient approximation (GGA) with the Perdew, Burke and Ernzerhof (PBE) parametrization;[46] and the DFT+U method, with PBE applied as the exchange-correlation functional, and a Hubbard on-site potential proposed by Dudarev *et al.*[47]

Within the DFT+U method, the potential energy is supplemented with a Hubbard-like term. For the present calculations, we employed the rotationally invariant approach proposed by Dudarev *et al.*,[47] where the correction for the on-site interactions between the Lu f electrons is expressed by a single $U_{\rm eff}$ parameter, where $U_{\rm eff} = U - J$, with U and J being screened Coulomb and exchange parameters, respectively. This energy term has the form

$$\mathrm{E_{DFT+U}} = \mathrm{E_{DFT}} + \frac{U-J}{2}\sum_{\sigma}\left[\mathrm{Tr}\left(\rho^{\sigma}(1-\rho^{\sigma})\right)\right]$$

where ρ is the 7×7 density matrix of the f states and σ denotes one of two spin orientations.[15] When setting $U_{\rm eff} = 0$ eV, one recovers the semi-local functional limit. $U_{\rm eff}$ is usually determined empirically, to fit some specific physical property, typically the band-gap width.[48]

The value for $U_{\rm eff}$ was chosen to be 5.4 eV, which is an adequate value in order to treat the localized f-states of the lanthanide systems (Refs. 14 and 17 for more details), whereas the $p-$ and $d-$states, constituting the upper valence-band and conduction-band, respectively, were treated at the PBE level.

The referenced methods are implemented in the Vienna *Ab-Initio* Simulation Package (VASP)[49–51] code, which performs electronic structure calculations by employing plane-wave basis sets to expand the Kohn-Sham wave-functions, thus taking advantage of the periodicity of extended systems. Projector Augmented Wave (PAW) pseudopotentials[52,53] were applied and the lower semi-core s and p shells of Lu were treated as valence electrons. Moreover, due to the nature of the two DFT approaches, two different sets of pseudopotentials for Lu were used: for the semi-local PBE calculations, the f-electrons are kept frozen inside the core region; whereas, for DFT+U, the f-states are reconstructed as part of the valence wavefunction.

For both methods, a plane-wave cut-off energy of 450 eV and an automatic mesh of $4 \times 4 \times 4$ Monkhorst-Pack grids[54] were applied. The total energies and the structural lattice relaxations were calculated by using these converged basis-sets. The lattice parameters (Sec. III) were obtained by fitting the Birch-Murningham equation of state to energy *vs* volume results.[55]

The formation energies of the hydrogen impurity, were evaluated in supercells of 80-atom structures of the host material. The formation energy of interstitial hydrogen is defined as the energy needed to incorporate the impurity in the host lattice and was determined for hydrogen in all the charge states $q = \{-1,\ 0,\ +1\}$ by following the procedure from Refs. 7, 33, 56, and 57. The corresponding expression is:

$$\mathrm{E_{form}(H^{\it q})} = \mathrm{E_{tot}(H^{\it q})} - \mathrm{E_{tot}(bulk)} - \frac{1}{2}\mathrm{E_{tot}(H_2)} + q(\mathrm{E_F} + E_{\rm VBM} + \Delta V).$$

$E_{tot}(H^q)$ is the total energy of the supercell with the hydrogen impurity of charge q, $E_{tot}(bulk)$ is the total energy of the bulk supercell and $\frac{1}{2}E_{tot}(H_2)$ is the reference energy for hydrogen that is given by an H_2 molecule at $T = 0$.[33,58] The Fermi level, E_F, is referenced to the valence-band maximum of the bulk supercell, E_{VBM}. ΔV denotes a correction term that aligns the average electrostatic potential of the defect supercell with that in the bulk[57] (and corresponds to the change of the reference potential after introducing a defect).

The use of supercells is a natural choice in solid state calculations, nevertheless one needs to take into account problems arising from charged defects incorporated in the system.[59] A neutralizing background charge needs to be introduced in order to cancel electrostatic divergences.[59] Image-type corrections based on multipole expansion were therefore added (up to the monopole-quadrupole interaction) to the total energies of the charged systems. These corrections were found to be in the range 0.1 eV to 0.2 eV.

The hyperfine coupling represents an interaction between the electron spin density $\sigma(\mathbf{r})$ with spin S, and nuclei J with nuclear spin I:

$$H = \sum_{i,j=1}^{3} S_i A_{ij} I_j$$

where i and j are the tensor components.

The hyperfine tensor, A_{ij} can be written as the sum of two interactions, a contact interaction (isotropic) and a classical interaction (anisotropic):[60]

$$A_{ij} = \frac{1}{2S}\gamma_J \gamma_e \hbar^2 \left[(A_{iso})_{ij} + (A_{ani})_{ij}\right]$$

γ_J is the nuclear Bohr magneton of nucleus J and γ_e the electron Bohr magneton.
The contact term, known as the Fermi-contact is defined as

$$(A_{iso})_{ij} = \frac{8\pi}{3}\delta_{ij}\int \delta(\mathbf{r}-\mathbf{R})\sigma(\mathbf{r})d\mathbf{r}$$

which is proportional to the magnitude of the electron spin density at the position of the nucleus. δ_{ij} represents the usual Kronecker delta (unit matrix).

The classical dipole-dipole contribution is:

$$(A_{ani})_{ij} = \int \left[\frac{3(\mathbf{r}-\mathbf{R})_i(\mathbf{r}-\mathbf{R})_j}{|\mathbf{r}-\mathbf{R}|^5} - \frac{\delta_{ij}}{|\mathbf{r}-\mathbf{R}|^3}\right]\sigma(\mathbf{r})d\mathbf{r}$$

More complete overview regarding the numerical implementation can be found in Refs. 60–62.

Convergence for the hyperfine parameters were obtained for a higher plane-wave cut-off of 550 eV with the same **k**-point sampling of $4 \times 4 \times 4$ Monkhorst-Pack grids.

The nuclear gyromagnetic ratios were taken from experimental values found at Ref. 63, with ^{1}H=42.577 MHz/T, ^{175}Lu=4.862 MHz/T and ^{16}O=0.000 MHz/T.

III. RESULTS AND DISCUSSION

Electronic Bulk Properties

The bulk properties were calculated by applying the two methods mentioned above. With PBE, we obtained a_0=10.37 Å as the lattice parameter value, whereas with DFT+U this value decreases to a_0=10.23 Å. The PBE result is comparable to experimental data found in Ref. 42, with a_0=10.39 Å. The DFT+U value is slightly lower, but compatible to other results obtained with the Hubbard-U approach (a_0=10.26 Å found in Ref. 15). It was argued that inclusion of the U term often tends to decrease the value of the lattice parameters.[15]

The calculated band-gap width, E_g=4.0 eV, is smaller than the value measured experimentally and found in the range 5.8-6.0 eV.[64,65] This is expected when employing the semi-local functional. Also, the inclusion of the Hubbard-U potential (which only acts on the f electrons) does not increase the magnitude of the gap since the latter is principally defined by the position of the valence p and conduction d states. The band gap obtained by DFT+U is therefore again equal to 4.0 eV. It is noteworthy to mention that an earlier study, by employing the DFT+U with a LDA functional, resulted in a smaller gap width (3.2 eV).[14]

The site and angular-momentum projected density of states (PDOS) (Fig. 2), provides a clear understanding of the effect of the Hubbard term upon the f-states. The upper valence-band of the oxide is formed by the O p-states, which are hybridized with the f-states of the metal. The conduction-band is formed mainly by metal d-stateswith a small contribution of O p-states. By setting U_{eff} = 0 eV, which is the limit of a purely PBE calculation, one observes that the f-states are completely delocalized within the p valence band. By increasing the Hubbard-U term, the f-states begin to localize and shift in energy towards more negative values. The value U_{eff} = 5.4 eV was found to be sufficient to localize the f-states below the p valence-band states, therefore not affecting the occupied-states that constitute the upper valence band. The width of the valence band is also observed to decrease when the f-states do not interact strongly with the p states.

Hydrogen Configurations and Formation Energy

Different initial interstitial hydrogen configurations were considered, by placing the H impurity at several positions in the lattice, near symmetry sites and different inequivalent void and unoccupied sites (Fig. 1). This was done for all charged states of hydrogen (H^+, H^- and H^0). Full structural relaxations were then carried out by both DFT and DFT+U.

Three stable configurations were found for H^0, in close analogy with those found in the isostructural Yttrium oxide.[32] One stable configuration exists for the interstitial

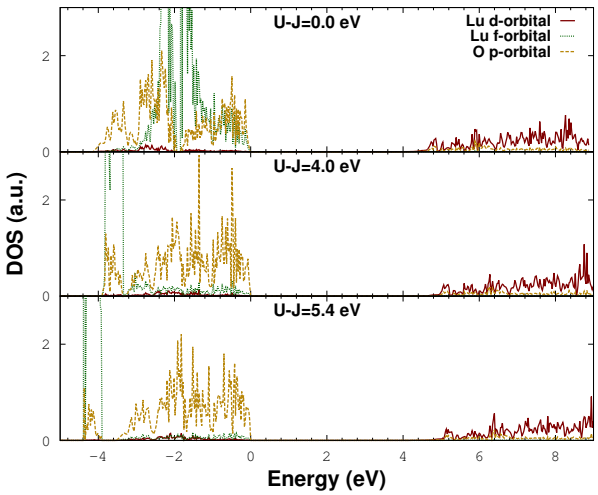

FIG. 2. (Color online) DFT+U partial site and angular momentum projected density of states of bulk Lu_2O_3. The three plots show the convergence of U_{eff} with respect to the overlap of f-states with p-O states, performed by defining $U_{\text{eff}} = 0.0$ eV, $U_{\text{eff}} = 4.0$ eV and $U_{\text{eff}} = 5.4$ eV. The valence-band maximum is aligned at the zero-energy level.

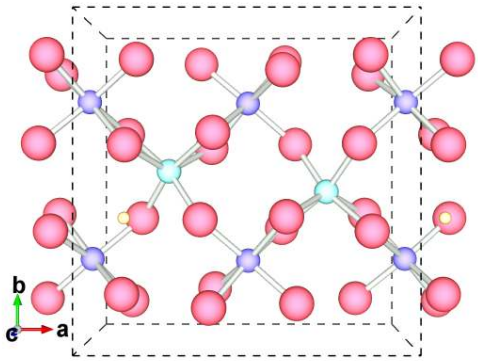

FIG. 3. (Color online) DFT+U stable H configuration for the H^0 and H^- states. The H impurity (represented by the small yellow sphere) stabilizes at an unoccupied O site.

unoccupied O site (unocc-O) and another for the interstitial void metal at the M_1-centre (void-M_1) (Figs. 3 and 4, respectively). The resulting relative energies between these two configurations imply that unocc-O is lower in energy than void-M_1, by either DFT or DFT+U.

A third stable H^0 configuration found is a bond O-H system (bond-O), where H binds to a O ion (Fig. 5). The energy of this bond configuration is higher when compared to the interstitial neutral configurations, a result predicted by both DFT and DFT+U methods.

The same configurations, with similar relative energy ordering, were found for the negatively-charged systems. In contrast, for the H^+ state, only the bond-O configurations are found as energy-minima. It is noteworthy that several nonequivalent bond-O configurations were obtained for either charge state; therefore, only the lowest-energy systems are discussed throughout the paper, and are taken as the representative systems for the respective charge states. Figs. 3, 4 and 5 were created by using the visualization program VESTA.[45]

For the bond-O neutral system, the impurity atom prefers to bind to an anion belonging to the equally distributed 6-fold mini-cube environment (void-M_2). On the other hand, for the charged states, H prefers to bond to a O belonging to a void-M_1 centre (bonded to the anion that sits at the 2-coordination face). (Fig. 5) The preferred configuration of the charged impurity will allow the lowering of steric effects which will in turn lower the overall energy cost due to the overlapping electron densities. The two O neighbour ions are brought closer together due to H interaction, by about 0.30 Å. The O-

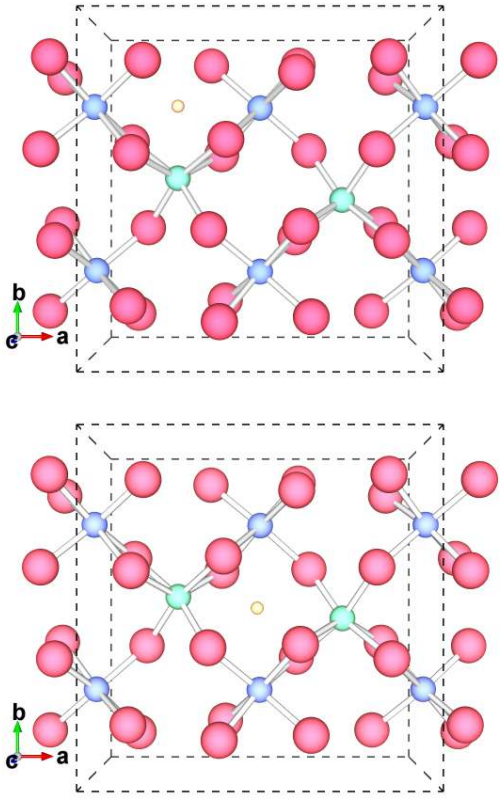

FIG. 4. (Color online) Stable H configuration for the H^0 and H^- states. The H impurity stabilizes at a void metal centre. The top plot represents the void-M_1 configuration (DFT+U) and the bottom plot the void-M_2 configuration (PBE). The latter configuration is only found at the PBE level for the neutral state and is not stable with DFT+U.

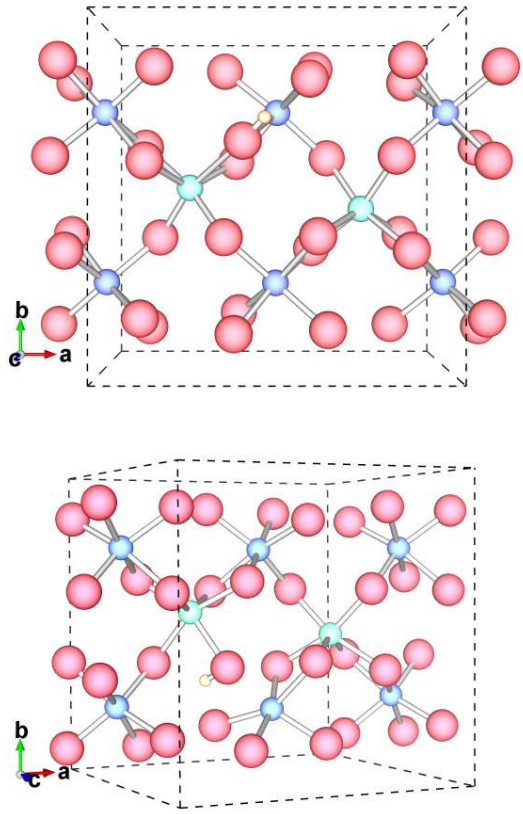

FIG. 5. (Color online) DFT+U bond-O configurations of the H impurity for the H^0 (top) and H^- (bottom) charge states. The stable configuration for the H^+ system is similar to the H^- state. The presented structures are the representative lowest-energy bond-O configurations.

H bond of the negatively charged system is 1.00 Å and the bond increases slightly for the positive charged system, up to 1.01 Å. For the neutral system, the length of the O-H bond is the same as the negatively charged system, about 1.00 Å of length. These configurations show a stronger lattice distortion, when compared to the interstitial H configurations, which is more pronounced for the positively charged states. At the close vicinity of the impurity center, several Lu-O bonds 'deform' from their original lengths in order to accommodate the perturbation caused by the impurity.

The stable configurations found by PBE and the DFT+U are structurally very similar. The only exception was that within PBE an additional impurity configuration was found for the neutral state: a void-M_2 state, which is represented in Fig. 4 (bottom). When employing DFT+U, this configuration is unstable with H displacing to the closest O unoccupied vertex.

The overall results for the formation energies are very similar, when comparison is made between the two methods: amphoteric behavior of H is found for the global ground-state energy structures. This compensating behavior can be understood based on the position of the charge-transition levels, $E(q/q')$, within the gap. Based on Figs 6, we observe that the pinning level, $E(+/-)$, is positioned in the middle of the band-gap. Also, a *negative-U* behaviour is observed since there is an inversion of the ordering of the levels: the donor level, $E(+/0)$, lies above the acceptor level, $E(0/-)$.[7,56] This suggests that the neutral configurations are never thermodynamically stable at any range of the Fermi-energy.

The energy ordering for the different impurity configurations is similar between the PBE and the DFT+U results, but it is clearly evidenced that the transition-levels for DFT+U are positioned at Fermi-level positions of higher energies (in the gap) (Fig. 6, bottom).

For both methods, the formation energies show that the most stable hydrogen configuration of the neutral and negative charged systems is at the unocc-O site. For the positive charged states, only the bond-O configuration exists, although it occurs with different surrounding environments. For the neutral and negatively charged systems, higher-energy configurations also occur, and the bond-O configurations are energetically less favourable for both charged systems than the configuration with hydrogen at the void-M_1 site (see Figs. 6). The fact that this bond-O configuration is higher in energy than the interstitial configurations is consistent with findings for other oxides, i.e. Yttria,[32] uranium oxide.[66] For PBE, the extra neutral configuration observed at the void-M_2 site is lower in energy (by about 0.17 eV) than that at the void-M_1 centre. This configuration is not stable using DFT+U, allowing to conclude that the valence contribution of the f-states has an influence in defining the configurational space of the impurity.

For PBE, the pinning level $E(+/-)$ lies deep in the gap, $E(+/-) = E_{\mathrm{VBM}} + 2.5$ eV, when aligned to the valence-band maximum (VBM). The donor level is positioned at $E(+/0) = E_{\mathrm{CBM}} - 0.2$ eV, which is very close to the conduction-band minimum (CBM), with the acceptor level located at $E(0/-) = E_{\mathrm{VBM}} + 1.1$ eV (Fig. 6). When employing DFT+U, the transition levels are shifted to higher energies, with $E(+/-) = E_{\mathrm{VBM}} + 2.9$ eV. The donor level, $E(0/+)$, of the lowest energy configuration, is thereby shifted to an energy level above the CBM, $E(+/0) = E_{\mathrm{CBM}} + 0.2$ eV, indicating that the electron in very loosely bound. Nonetheless, the pinning level is not sufficiently above (or close enough) to the CBM, to allow for hydrogen to be a source of doping.[7]

For the higher energy, bond-O, configurations, the respective pinning and the donor levels lie above the CBM (observed for both methods). From these results we can infer that a portion of these bond-type configurations are shallow donor-like configurations with corresponding donor and pinning levels interacting with the CB states.

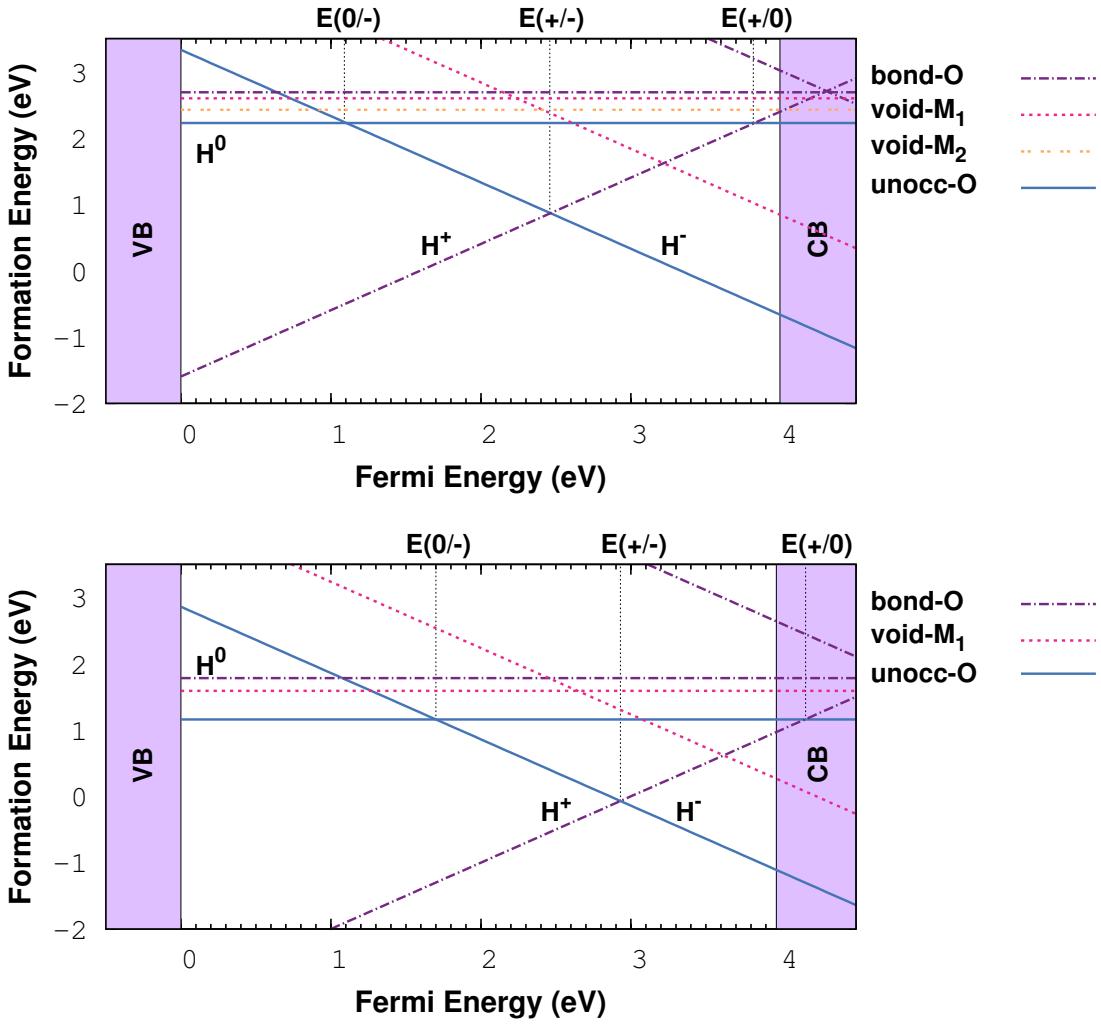

FIG. 6. (Color online) Formation energy of the different hydrogen configurations as a function of the Fermi-level position. The range of E_F corresponds to the bulk theoretical band-gap with E_F=0 aligned at the valence-band maximum. The formation energies of the different geometrical configurations are represented by different line types and colors. The upper plot represents the results obtained by employing the PBE exchange-correlation functional, where the f-electrons were treated as core-like states. The lower plot represents the results obtained from DFT+U with the f-electrons treated as valence-states. The thermodynamic charge-transition (electrical) levels are marked by the vertical lines.

Local Density of States and Electron-Density Isosurfaces

In order to probe the character of the defect-induced levels inside the gap, the site and angular-momentum projected (PDOS) of the different neutral geometrical configurations were evaluated, by employing both levels of theory (Figs. 7, 8 and 9). Since spin-polarised calculations were carried out the PDOS plots display both spin-channel components.

For the unocc-O and void-M_1 configurations, the defect levels are positioned quite close to the valence-band (depicted in Figs. 7 and 8). For the unocc-O configuration, and by applying DFT+U, the impurity level is located 0.3 eV above the VBM, and for PBE it is 0.2 eV (considering the spin-up states, where the impurity level is closest to the VBM). For the void-M_1 configuration, the level is positioned at higher energies, although still close to the VBM - 1.4 eV and 1.3 eV for DFT+U and PBE, respectively.

Conversely, the oxygen-bond configurations differ from the unoccupied and void configurations. By looking at the PBE results, it is not possible to observe a defect level inside the gap (Fig. 9). However, for DFT+U, a small level (mainly of p and d contribution, and very low portion due to s-states), is positioned inside the gap, and very close to the CBM ($\sim$ 0.2 eV below the CBM, with the DFT+U bulk band-gap being of the order of $\sim$ 4.0 eV). One may observe that a very low concentration of s-states of the impurity is delocalized at the CB. This

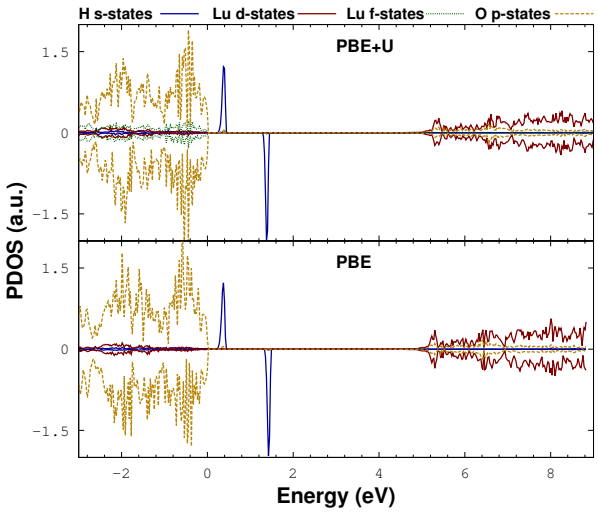

FIG. 7. (Color online) Spin-polarised partial site and angular momentum projected density of states of the unocc-O configuration calculated by employing DFT+U (top) and PBE (bottom). The valence-band maximum is aligned at the zero-energy level.

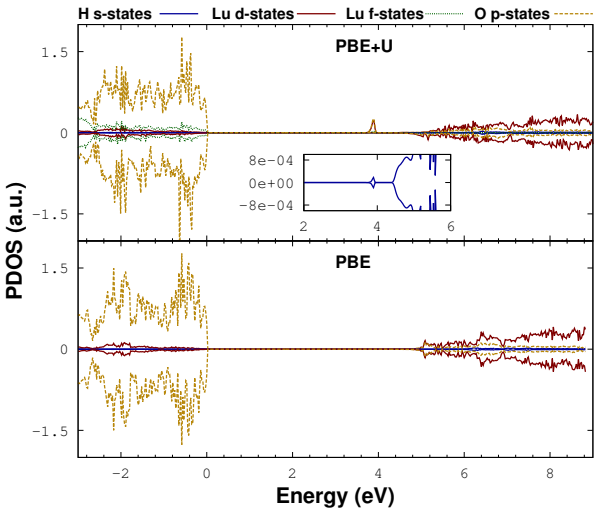

FIG. 9. (Color online) Partial site and angular momentum projected density of states of the lowest energy bond-O configuration calculated by employing DFT+U (top) and PBE (bottom). The valence-band maximum is aligned at the zero-energy level.

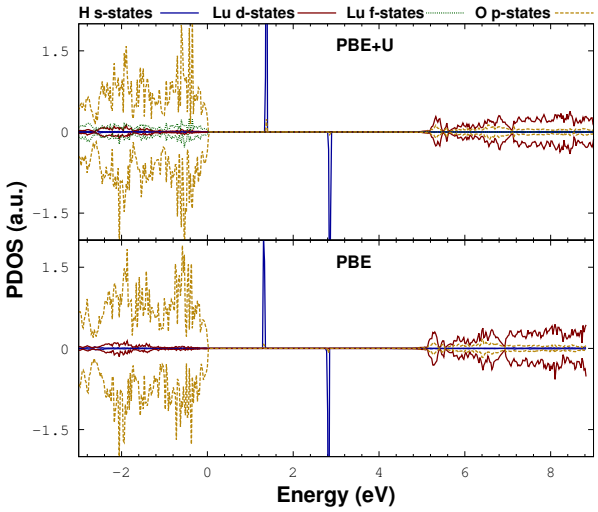

FIG. 8. (Color online) Spin-polarised partial site and angular momentum projected density of states of the stable void-M_1 configuration calculated by employing DFT+U (top) and PBE (bottom). The valence-band maximum is aligned at the zero-energy level.

feature may suggest that the impurity electron is loosely bound to H, allowing for the impurity to act as a shallow-donor.

The electron-density isosurfaces of the neutral systems were evaluated with DFT+U, in order to provide a more detailed information regarding the nature and localization of the impurity electron.

For the unocc-O and the void-M_1 configurations, where a defect level is positioned close to the VBM (Fig. 10), one may observe that the isosurfaces possess a strong s-type character with the electron centred at the impurity. Contributions of p-states around the impurity, on the next-neighbour O anions (depicted in Fig. 10), are also seen and justified from the close proximity of the defect level to the valence-band edge, which has essentially p-character (Fig. 7).

For the bond-O systems, and similarly to what was found in Ref. 32 for yttria and in Ref. 34 for cubic zirconia, one may observe that the hydrogen electron is trapped at the closest cation neighbours (Fig. 11). In response to the formation of the impurity-anion bond, significant lattice distortion takes place for these configurations. These are related to a change of oxidation state of the corresponding anion (O^{2-} to OH^{-} state) causing the lengths of the neighbouring bonds to adjust, thus resulting in large rearrangements of the host lattice.[67]. The resulting displacement field near the hydrogen impurity causes the defect electron to become trapped close to the impurity atom, at a cation centre.[68] This behavior resembles the effects suggested by Cox *et al.*[68] of a polaron-type formation, where the polaron-center may be shallow and therefore act as a donor-centre as well. The impurity electron is trapped close to the hydrogen nucleus, at nearby metal centres, and has predominantly a conduction-band d-type character - the defect-level is positioned quite close to the conduction-band allowing the respective states to interact with each other (Fig. 11).

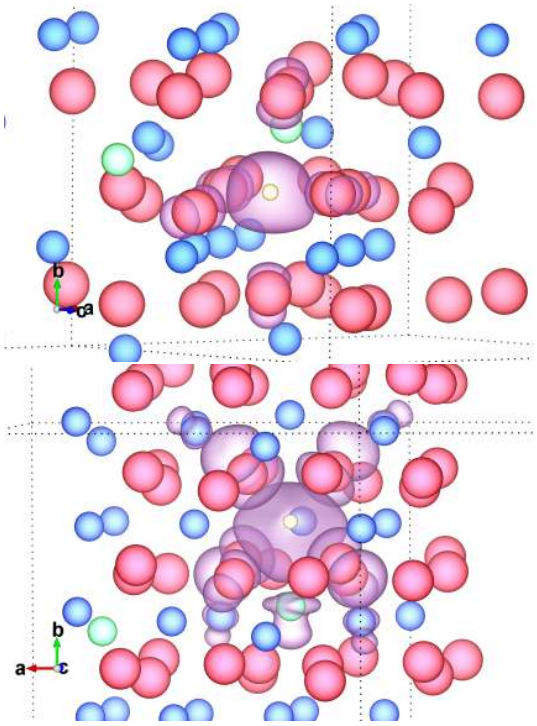

FIG. 10. (Color online) DFT+U isosurfaces of the electron charge densities for the neutral state of unocc-O and void-M_1 configurations. The atoms are represented by their ionic radius, where O is depicted in red, Lu in blue/green and hydrogen in yellow.

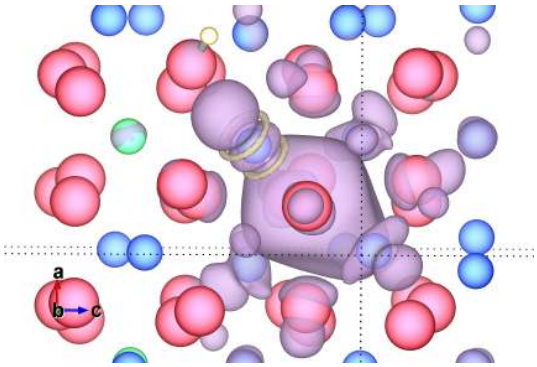

FIG. 11. (Color online) DFT+U isosurfaces of the electron charge densities for the neutral state of the representative, lowest energy, bond-O configuration. The atoms are represented by their ionic radius, where O is depicted in red, Lu in blue/green and hydrogen in yellow. The purple color of the isosurface refers to positive values and the yellow to negative values.

Hyperfine Constants

The calculations of the hyperfine tensors proved useful in characterizing the neutral impurity centers, thus allowing a direct comparison with the experimentally obtained hyperfine constants measured by μSR. Only the DFT+U method was employed in this case, since it is within this level of theory that the f-orbitals are treated correctly as valence states. Moreover, it is also well known that a pure PBE approach tends to delocalise the spin-density of defect-centres.[60]

The calculations for the neutral interstitial hydrogen configurations (hydrogen at the unoccupied unocc-O and void-M_1 sites) revealed a predominant isotropic component with very small dipolar part. The Fermi-contact isotropic constant, $A_{\rm iso}$, was found equal to be 926 MHz and 1061 MHz for the unocc-O and void-M_1 configurations, respectively. These results indicate that it is the latter configuration which yields a higher spin localization.

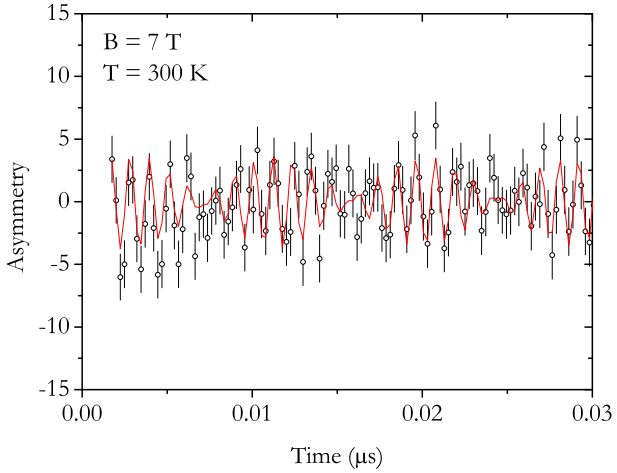

FIG. 12. (Color online) μSR time spectrum of a polycrystalline sample of Lu_2O_3, for an applied transverse magnetic field $B = 7$ T, at $T = 300$ K. The beating of the diamagnetic frequency and of the muonium ν_{12} line is clearly seen. The red line is a fit as described in the text.

μSR results and analysis

The oxide sample used in the present study was obtained commercially from Alfa-Aesar; REActon 99.995%. The measurements were performed with the HiTime spectrometer on the M15 surface muon channel at TRIUMF (Vancouver, Canada).

The μSR spectrum at $T = 300$ K, for an external applied magnetic field $B = 7$ T, is shown in Fig. 12. A clear oscillating pattern is observed, which corresponds to the beating between two frequencies identified at $\nu_d = 948.96(2)$ MHz and at $\nu_{12} = 833.2(2)$ MHz. The corresponding Fast-Fourier Transform (FFT) is shown in Fig. 13. ν_d corresponds to the expected Larmor frequency of the diamagnetic muon at the applied field. ν_{12} is a frequency characteristic of the $1 \rightarrow 2$ transition in the field-dependent hyperfine spectrum of muonium, the paramagnetic bound state of a positive muon with an electron. In the high-field limit, this frequency cor-

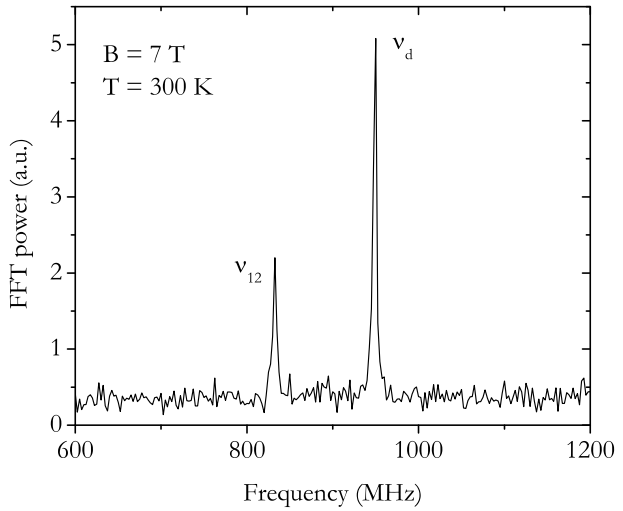

FIG. 13. (Color online) Fast-Fourier transform (FFT) of the μSR time spectrum at room temperature, for an applied transverse magnetic field $B = 7$ T, showing the presence of the diamagnetic frequency at $\nu_d = 948.98(1)$ MHz and of the muonium ν_{12} frequency at $\nu_{12} = 833.2(2)$ MHz.

responds to the "flip" of the muon spin with electron spin up and amounts to half of the spectral weight.[38] The other half of the spectral weight corresponds to the unobservable ν_{34} frequency characteristic of the $3 \rightarrow 4$ transition where the muon spin "flips" with electron spin down.

The time spectrum in Fig. 12 was thus analysed using a sum of damped oscillations of the form:

$$A(t) = A_{dia} e^{-\lambda_{dia} t} \cos\left(2\pi\nu_{dia} t + \phi_{dia}\right) + A_{Mu} e^{-\lambda_{Mu} t} \cos\left(2\pi\nu_{Mu} t + \phi_{Mu}\right)$$

A room temperature calibration with a silver sample at $B = 7$ T allowed to extract the maximum instrumental asymmetry A_{max} and therefore to measure the fraction of muons thermalizing at the diamagnetic configuration ($f_{dia} = A_{dia}/A_{max}$) and the fraction of muons thermalizing at the paramagnetic muonium configuration ($f_{Mu} = 2A_{Mu}/A_{max}$, where the multiplication by two accounts for the unobservable υ_{34} transition). We find that $f_{dia} = 23(1)\%$ and $f_{Mu} = 46(3)\%$. The corresponding relaxations were found to be $\lambda_{dia} = 0.1(1)\,\mu\,s^{-1}$ and $\lambda_{Mu} = 6(1)\,\mu\,s^{-1}$.

We begin the discussion of the experimental data by noting that the experimental observations are consistent with the presence of an isotropic hyperfine interaction. From the fitted value of ν_{12} we can easily estimate the value of the hyperfine interaction[38,69] to be $A_{\rm iso} = 3596.7(4)$ MHz. We have confirmed that ν_{12} varies as expected for this hyperfine interaction by performing room-temperature measurements at $B = 2$ T and at $B = 4$ T, obtaining $\nu_{12} = 1470.4(5)$ MHz and $\nu_{12} = 1227.7(5)$ MHz, respectively. Both are consistent with $A_{\rm iso} = 3597(1)$ MHz.

In order to compare this value with the calculated values for hydrogen, we must take into account that the hyperfine interaction for muonium is expected to be higher than that for hydrogen by the factor 3.184 corresponding to the ratio of the magnetic moment of the muon and that of the proton.[40] The expected value for the experimentally-measured hyperfine interaction, taking the correction into account, is equal to $A_{\rm iso} = 1129.7(3)$ MHz. This means that the calculated values for the unocc-O and void-M_1 interstitial configurations (see previous subsection) are lower than the experimental value by 18% and 6%, respectively. These discrepancies are judged satisfactory given the approximate treatment of exchange and on-site correlation adopted in the present work.

In fact, similar discrepancies have also been reported recently between the hyperfine interactions calculated by *ab-initio* methods and those measured experimentally.[60] These authors report differences of about 15% to 20% in the calculation of hyperfine interactions in solids using the PBE functional, which notably decrease when using a hybrid-functional (HSE06) approach. Also (and more in relevance to the present work), in a recent study[70] of hyperfine parameters of neutral hydrogen configurations in zirconia, the isotropic constants calculated within PBE were smaller to those obtained by HSE06 by as much as 10 % (for a fixed plane-wave cutoff energy). Taking into account that the calculated values of the hyperfine interactions for the unocc-O and void-M_1 interstitial configurations are themselves different by less than 15%, it is not possible to assign the experimentally observed muonium state to a specific configuration from the value of the hyperfine interaction alone. The observed value is nevertheless consistent with the calculated values. It is also important to note that a slight variation of the value of the hyperfine interaction of muonium with respect to that of hydrogen is expected due to the different zero-point motion of the muon and of the proton.

A measurement at 2.5 K indicates that the same isotropic state is present at low-temperatures, albeit with a smaller fraction ($\sim 20\%$) and a slightly larger hyperfine interaction $A_{\rm iso} = 3629(2)$ MHz, corresponding to $A_{\rm iso} = 1139.8(6)$ MHz after taking the referred magnetic moment ratio into account. The investigation of the corresponding temperature dependence is ongoing and will be published elsewhere. We however note that the slight decrease of the hyperfine interaction with increasing temperature is a well known effect of the onset of lattice vibrations.[38,69] The different formation probability also relate to the muonium formation process and is a temperature-dependent process.[71–73] The increase of the formation probability of the observed muonium state with increasing temperature is reflected in the corresponding decrease of the unobservable fraction of muon spin polarization (missing fraction), the diamagnetic fraction remaining sensibly constant. This missing

fraction is associated to muons whose spin polarization is lost during the thermalization process and therefore reflects the presence of another paramagnetic state, either as a precursor or as a final state.[71–73]

The diamagnetic fraction is likely associated to muons thermalizing as Mu^+ in oxygen-bond configurations and the large missing fraction is probably associated to the formation of muonium in the lower-energy interstitial sites.

In short, these results basically reveal the formation of an atom-like muonium configuration with an hyperfine interaction of 3629(2) MHz at low temperatures, in line with the calculated values for any of the interstitial positions of hydrogen in Lu_2O_3. Together with the muonium state directly observable spectroscopically, there is evidence of the presence of another atom-like state, possibly a precursor configuration. Although the experimental data do not provide a direct identification of the muonium site corresponding to the directly observed state, it possibly corresponds to muonium thermalizing at the ground state configuration in the unocc-O site. The understanding of the muonium formation process in Lu_2O_3 is likely to allow a more definitive assignment.

IV. CONCLUSIONS

Calculations of the H impurity were carried out in Lu_2O_3 by employing two levels of theory: DFT with the semi-local PBE functional and DFT+U. Whereas within the semi-local approximation the f-states of Lu are taken as being core-states, with the DFT+U these are correctly treated as localized valence states.

Results between the two methods predict similar stable configurations for the impurity, with the neutral H impurity stabilizing at an unoccupied O site, unocc-O, and to a void metal centre, void-M_1. The former is lower in energy and therefore the ground-state configuration in the lanthanide oxide. An higher-energy configuration is also predicted, where the hydrogen binds to a neighbour anion O, bond-O configuration. The negative charged systems also indicate a similar energetic stability of the three mentioned configurations. On the other hand, the bond-O configurations are the only possible configurations for the positively charged systems.

From the formation energies, we observed that by taking into account the lowest-energy configurations of the three charge states of H, amphoteric behavior is predicted. DFT+U calculations show that the donor level is positioned above the CBM and the pinning level inside the gap. This indicates that despite its compensating character, the H electron at the donor configuration is loosely bound to the impurity atom. By comparison, and considering the metastable bond-O configurations (of the three charge states), we observe both pinning-level and donor level above the CBM. On the other hand, the plotted isosurfaces of the neutral bond-O configuration indicates a polaron-type character, where the electron from the impurity is trapped at a metal centre, and interacting with a portion of the conduction-band states.

The hyperfine interactions have been calculated for the neutral interstitial (unocc-O and void-M_1) configurations of hydrogen leading to isotropic (Fermi-contact) constant equal to 926 and 1061 MHz, respectively. These results are in good agreement with the measurements of muonium spectroscopy which infer a neutral fraction with a strong isotropic hyperfine interaction of similar magnitude.

ACKNOWLEDGMENTS

This work was supported with funds from (i) FEDER (Programa Operacional Factores de Competitividade COMPETE) and from FCT - Fundação para a Ciência e Tecnologia under projects PEst-OE/FIS/UI0036/2014 and PTDC/FIS/102722/2008; (ii) PhD grant SFRH/BD/87343/2012 from FCT - Fundação para a Ciência e Tecnologia (RBLV); (iii) Welch Foundation grant D-1321 (TTU group). The authors would also like to thank the computing support from the Department of Physics at the Laboratory for Advanced Computing of the University of Coimbra and from the Department of Chemistry of the University of Bath. Acknowledgements are also to be made to Dr. Marco Molinari of the Department of Chemistry, University of Bath, for fruitful discussions. The technical help of the μSR team at TRIUMF is gratefully acknowledged.

* elds22@bath.ac.uk

[1] G. Adachi, N. Imanaka, and Z. C. Kang. *Binary Rare Earth Oxides*, chapter 9. Kluwer Academic Publishers, Dordrecht, 2004.

[2] J. Robertson. High Dieletric Constant Gate Oxides for Metal Oxide Si Transistors. *Reports on Progress in Physics*, 69:327 – 396, 2006.

[3] P. W. Peacock and J. Robertson. Band Offsets and Schottky Barrier Heights of High Dielectric Constant Oxides. *Journal of Applied Physics*, 92:4712, 2002.

[4] L. Tsetseris, D. M. Fleetwood, R. D. Schrimpf, and S. T. Pantelides. *Defects in Microelectronic Materials and Devices*, chapter 13, pages 381 – 398. CRC Press Taylor & Francis Group, LLC, 2009.

[5] J. Robertson, K. Xiong, and K. Tse. *Defects in Microelectronic Materials and Devices*, chapter 9, pages 283 – 303. CRC Press Taylor & Francis Group, LLC, 2009.

[6] K. Xiong J. Robertson and S. J. Clark. *Defects in High-K Gate Dielectric Stacks*, pages 175 – 187. Springer, 2006.

[7] C. G. Van de Walle and J. Neugebauer. Hydrogen in Semiconductors. *Annu. Rev. Mater. Res.*, 36:179 – 98, 2006.

[8] R. Alvero, A. Bernal, I. Carrizosa, J. A. Odriozola, and

J. M. Trillo. Lanthanide Oxides: Lu_2o_3 Hydration. *Journal of the Less Common Metals*, 110(1–2):425, 1985.

[9] C. G. Van de Walle. Hydrogen as a Cause of Doping in Zinc Oxide. *Physical Review Letters*, 85:1012, 2000.

[10] C. G. Van de Walle, P. J. H. Denteneer, Y. Bar-Yam, and S. T. Pantelides. Theory of hydrogen diffusion and reactions in crystalline silicon. *Physical Review B*, 39:10791, 1989.

[11] T. Norby and P. Kofstad. Proton and Native-Ion conductivities in Y_2O_3 at High Temperatures. *Solid State Ionics*, 20:169 – 184, 1986.

[12] T. Norby and P. Kofstad. Electrical Conductivity of Y_2O_3 as a Function of Oxygen Partial Pressure in Wet and Dry Atmospheres. *Journal of the American Ceramic Society*, 69:784 – 789, 1986.

[13] H. Li and J. Robertson. Behaviour of Hydrogen in Wide Band Gap Oxides. *Journal of Applied Physics*, 115(20):203708, May 2014.

[14] H. Jiang, P. Rinke, and M. Scheffler. Electronic Properties of Lanthanide Oxides from the GW Perspective. *Physical Review B*, 86:125115, 2012.

[15] L. Ning, Y. Zhang, and Z. Cui. Structural and Electronic Properties of Lutecia from First Principles. *Journal of Physics: Condensed Matter*, 21:455601, 2009.

[16] R. Gilland, S. J. Clark, and J. Robertson. Nature of the Electronic Band Gap in Lanthanide Oxides. *Physical Review B*, 87:125116, 2013.

[17] H. Jiang, R. I. Gomez-Abal, P. Rinke, and M. Scheffler. Localized and Itinerant States in Lanthanide Oxides United by *GW*@LDA+U. *Physical Review Letters*, 102:126403, 2009.

[18] B. Huang, R. Gilland, and J. Robertson. Study of CeO_2 and Its Native Defects by Density Functional Theory with Repulsive Potential. *Journal OF Physical Chemistry C*, 118:24248, 2014.

[19] K. Hummler and M. Fähnle. Full-Potential Linear-Muffin-Tin-Orbital Calculations of the Magnetic Properties of Rare-Earth–Transition-Metal Intermetallics. I. Description of the Formalism and Application to the Series RC_{O_5} (R=Rare-Earth Atom). *Phyiscal Review B*, 53:3272, 1996.

[20] N. Hirosaki, S. Ogata, and C. Kocer. Ab initio Calculation of the Crystal Structure of the Lanthanide Ln_2O_3 Sesquioxides. *Journal of Alloys and Compounds*, 351:31, 2003.

[21] K. Xiong and J. Robertson. Behavior of hydrogen in wide band gap oxides. *Journal of Applied Physics*, 102:083710, 2007.

[22] Matthew D. McCluskey, Marianne C. Tarun, and Samuel T. Teklemichael. Hydrogen in Oxide Semiconductors. *Journal of Materials Research*, 27:2190, 2012.

[23] Detlev M. Hofmann, Albrecht Hofstaetter, Frank Leiter, Huijuan Zhou, Frank Henecker, Bruno K. Meyer, Sergei B. Orlinskii, Jan Schmidt, and Pavel G. Baranov. Hydrogen: A Relevant Shallow Donor in Zinc Oxide. *Physical Review Letters*, 88(4):045504, 2002.

[24] A. T. Brant, Shan Yang, N. C. Giles, and L. E. Halliburton. Hydrogen Donors and $Ti3^+$ ions in Reduced TiO_2 Crystals. *Journal of Applied Physics*, 110(5):053714, 2011.

[25] F. Herklotz, E. V. Lavrov, and J. Weber. Infrared Absorption of the Hydrogen Donor in Rutile Tio_2. *Physical Review B*, 83:235202, 2011.

[26] F. Bekisli, W. Beall Fowler, and M. Stavola. Small Polaron Characteristics of an OD Center in TiO_2 Studied by Infrared Spectroscopy. *Physical Review B*, 86:155208, Oct 2012.

[27] S. F. J. Cox, R. L. Lichti, J. S. Lord, E. A. Davis, R. C. Vilão, J. M. Gil, T. D. Veal, and Y. G. Celebi. The First 25 Years of Semiconductor Muonics at ISIS, Modelling the Electrical Activity of Hydrogen in Inorganic Semiconductors and High-κ Dielectrics. *Physica Scripta*, 88:068503, 2013.

[28] R. C. Vilão, J. M. Gil, A. Weidinger, H. V. Alberto, J. Piroto Duarte, N. Ayres de Campos, R. L. Lichti, K. H. Chow, and S. F. J. Cox. Information on Hydrogen States in II–VI Semiconductor Compounds from a Study of their Muonium Analogues. *Nuclear Instruments and Methods in Physics Research Section A*, 580(1):438, 2007.

[29] R. C. Vilão, A. G. Marinopoulos, R. B. L. Vieira, A. Weidinger, H. V. Alberto, J. Piroto Duarte, J. M. Gil, J. S. Lord, and S. F. J. Cox. Hydrogen Impurity in Paratellurite α-TeO_2: Muon-Spin Rotation and Ab Initio Studies. *Physical Review B*, 84(4):045201, July 2011.

[30] R. B. L. Vieira, R. C. Vilão, P. M. Gordo, A. G. Marinopoulos, H. V. Alberto, J. Piroto Duarte, J. M. Gil, A. Weidinger, and J. S. Lord. Muon-Spin-Rotation Study of Yttria-Stabilized Zirconia (ZrO_2:Y): Evidence for Muon and Electron Separate Traps. *Journal of Physics: Conference Series*, 551(1):012050, 2014.

[31] R.L. Lichti, K.H. Chow, J.M. Gil, D.L. Stripe, R.C. Vilão, and S.F.J. Cox. Location of the H Level: Experimental Limits for Muonium. *Physica B: Condensed Matter*, 376–377:587, 2006. Proceedings of the 23rd International Conference on Defects in Semiconductors.

[32] E. L. Silva, A. G. Marinopoulos, R. C. Vilão, R. B. L. Vieira, H. V. Alberto, J. Piroto Duarte, and J. M. Gil. Hydrogen Impurity in Yttria: Ab initio and μSR Perspectives. *Physical Review B*, 85:165211, 2012.

[33] Proceedings of the 23rd International Conference on Defects in Semiconductors. *Universal Alignment of Hydrogen Levels in Semiconductors and Insulators*, volume 376-377, 2006.

[34] A. G. Marinopoulos. Incorporation and Migration of Hydrogen in Yttria-Stabilized Cubic Zirconia: Insights from Semilocal and Hybrid-Functional Calculations. *Physical Review B*, 86:155144, 2012.

[35] J. S. Lord, S. F. J. Cox, H. V. Alberto, J. Piroto Duarte, and R. C. Vilão. Double-Resonance Determination of Electron g-Factors in Muonium Shallow-Donor States. *Journal of Physics: Condensed Matter*, 16(40):S4707, 2004.

[36] J. S. Lord, S. P. Cottrell, P. J. C. King, N. Alberto, H. V .and Ayres de Campos, J. M. Gil, J. Piroto Duarte, R. C. Vilão, R. L. Lichti, S. K. L. Sjue, B. A. Bailey, A. Weidinger, E. A. Davis, and S. F. J. Cox. Probing the Shallow-Donor Muonium Wave Function in ZnO and CdS via Transferred Hyperfine Interactions. *Physica B: Condensed Matter*, 308 - 310(0):920, 2001.

[37] J. M. Gil, H. V. Alberto, R. C. Vilão, J. Piroto Duarte, N. Ayres de Campos, A. Weidinger, J. Krauser, E. A. Davis, S. P. Cottrell, and S. F. J. Cox. Shallow Donor Muonium States in II-VI Semiconductor Compounds. *Physical Review B*, 64(7):075205, 2001.

[38] R. C. Vilão, H. V. Alberto, J. Piroto Duarte, J. M. Gil, A. Weidinger, N. Ayres de Campos, R. L. Lichti, K. H. Chow, and S. F. J. Cox. Muonium Spectroscopy in ZnSe: Metastability and Conversion. *Physical Review B*, 72:235203, Dec 2005.

[39] J. M. Gil, H. V. Alberto, R. C. Vil ao, J. Piroto Duarte, N. Ayres de Campos, A. Weidinger, E. A. Davis, and

S. F. J. Cox. Muonium States in HgO. *Journal of Physics: Condensed Matter*, 13(27):L613, 2001.

[40] R. C. Vilão, R. B. L. Vieira, H. V. Alberto, J. M. Gil, A. Weidinger, R. L. Lichti, B. B. Baker, P. W. Mengyan, and J. S. Lord. Muonium Donor in Rutile TiO_2 and comparison with Hydrogen. *Physical Review B*, 92:081202, Aug 2015.

[41] F. L. Pratt. WIMDA: A Muon Data Analysis Program for the Windows PC. *Physica B*, 289-290:710, 2000.

[42] R. Wyckoff. *Crystal Structures*, volume 1. Wiley, New York, 1963.

[43] P. Villars and L. D. Calvert. *Pearson's Handbook of Crystallographic Data for Intermetallic Phases*, volume IV. 2nd Edition, ASM International, Materials Park, Ohio, 1991.

[44] Y.-N. Xu, Z.-Q. Gu, and W. Y. Ching. Electronic, Structural, and Optical Properties of Crystalline Yttria. *Physical Review B*, 56:14993, 1997.

[45] K. Momma and F. Izumi. VESTA: A Three-Dimensional Visualization System for Electronic and Structural Analysis. *Journal of Applied Crystallography*, 41:653, 2008.

[46] J. P. Perdew, K. Burke, and M. Ernzerhof. Generalized Gradient Approximation made Simple. *Physical Review Letters*, 77:3865, 1996.

[47] S. L. Dudarev, G. A. Botton, S. Y. Savrasov, C. J. Humphreys, and A. P. Sutton. Electron-Energy-Loss Spectra and the Structural Stability of Nickel Oxide: An LSDA+U Study. *Physical Review B*, 57:1505, 1998.

[48] S. Lutfalla, V. Shapovalov, and A. T. Bell. Calibration of the DFT/GGA+U Method for Determination of Reduction Energies for Transition and Rare Earth Metal Oxides of Ti, V, Mo, and Ce. *Journal of Chemical Theory and Computation*, 7:2218, 2011.

[49] G. Kresse and J. Furthmüller. Efficient Iterative Schemes for *Ab Initio* Total-Energy Calculations using a Plane-Wave Basis Set. *Physical Review B*, 54:11169, 1996.

[50] G. Kresse and J. Hafner. Ab Initio Molecular Dynamics for Liquid Metals. *Physical Review B*, 47:R558, 1993.

[51] G. Kresse and J. Furthmüller. Efficiency of Ab-Initio Total Energy Calculations for Metals and Semiconductors using a Plane-Wave Basis Set. *Comput. Mat. Sci.*, 6:15, 1996.

[52] G. Kresse and D. Joubert. From Ultrasoft Pseudopotentials to the Projector Augmented-Wave Method. *Physical Review B*, 59:1758, 1999.

[53] P. E. Blöchl. Projector Augmented-Wave Method. *Physical Review B*, 50:17953, 1994.

[54] H. J. Monkhorst and J. D. Pack. Special Points for Brillouin-Zone Integrations. *Phyiscal Review B*, 13:5188, 1976.

[55] F. D. Murnaghan. The Compressibility of Media under Extreme Pressures. *Proc. Natl. Acad. Sci.*, 30:244, 1944.

[56] C. G. Van de Walle and J. Neugebauer. Universal Alignment of Hydrogen Levels in Semiconductors, Insulators and Solutions. *Nature*, 423:626, 2003.

[57] C. G. Van de Walle and J. Neugebauer. First-Principles Calculations for Defects and Impurities: Applications to III-Nitrides. *Journal of Applied Physics*, 95:3851, 2004.

[58] C. G. Van de Walle. Theory of Hydrogen-Related Levels in Semiconductors and Oxides. In *Electron Devices Meeting, 2005*, page 403. IEDM Technical Digest. IEEE International, 2005.

[59] R. M. Nieminen. Issues in First-Principles Calculations for Defects in Semiconductors and Oxides. *Modelling and Simulation in Materials Science and Engineering*, 17:084001, 2009.

[60] Krisztián Szász, Tamás Hornos, Martijn Marsman, and Adam Gali. Hyperfine Coupling of Point Defects in Semiconductors by Hybrid Density Functional Calculations: The Role of Core Spin Polarization. *Physical Review B*, 88:075202, Aug 2013.

[61] VASPwiki. http://cms.mpi.univie.ac.at/wiki/.

[62] O. V. Yazyev, I. Tavernelli, L. Helm, and U. Röthlisberger. Core Spin-Polarization Correction in Pseudopotential-Based Electronic Structure Calculations. *Physical Review B*, 71:115110, Mar 2005.

[63] webElements. http://www.webelements.com.

[64] M. Perego, G. Seguini, G. Scarel, and M. Fanciulli. X-ray Photoelectron Spectroscopy Study of Energy-Band Alignments of Lu_2O_3 on Ge. *Surface and Interface Analysis*, 38:494 – 497, 2006.

[65] T. Hattori, T. Yoshida, T. Shiraishi, K. Takahashi, H. Nohira, S. Joumori, K. Nakajima, M. Suzuki, K. Kimura, I. Kashiwagi, C. Ohshima, S. Ohmi, and H. Iwai. Composition, Chemical Structure, and Electronic Band Structure of Rare Earth Oxide/Si(1 0 0) Interfacial Transition Layer. *Microelectronic Engineering*, 72:283, 2004.

[66] J. M. Flitcroft, M. Molinari, N. A. Brincat, M. T. Storrb, and S. C. Parker. Hydride Ion Formation in Stoichiometric UO_2. *Chemical Communications*, 51:16209, 2015.

[67] P. A. Cox. *Transition Metal Oxides*, chapter 2. Clarendon Press, Oxford, 1992.

[68] S. F. J. Cox, J. L. Gavartin, J. S. Lord, S. P. Cottrell, J. M. Gil, H. V. Alberto, J. P. Duarte, R. C. Vilão, N. A. de Campos, D. J. Keeble, E. A. Davis, M. Charlton, and D. P. van der Werf. Oxide Muonics: II. Modelling the electrical activity of hydrogen in wide-gap and high-permittivity dielectrics. *Journal of Physics: Condensed Matter*, 18:1079, 2006.

[69] Bruce D. Patterson. Muonium States in Semiconductors. *Rev. Mod. Phys.*, 60:69, Jan 1988.

[70] A. G. Marinopoulos. First Principles Study of Hydrogen Configurations at the core of a High Angle Grain Boundary in Cubic Yttria Stabilized Zirconia. *Journal of Physics: Condensed Matter*, 26:025502, 2014.

[71] H. V. Alberto, A. Weidinger, R. C. Vilão, J. Piroto Duarte, J. M. Gil, J. S. Lord, and S. F. J. Cox. Mechanisms of Electron Polarization of Shallow Muonium in CdTe and CdS. *Physical Review B*, 81:245205, Jun 2010.

[72] H. V. Alberto, R. C. Vilão, J. Piroto Duarte, J. M. Gil, A. Weidinger, J. S. Lord, and S. F. J. Cox. Electron Polarization and Formation Probability of Bound Muonium in CdS and Si. *Physical Review B*, 86:035203, Jul 2012.

[73] R. B. L. Vieira, R. C. Vilão, H. V. Alberto, J. M. Gil, A. Weidinger, B. B. Baker, P. W. Mengyan, and R. L. Lichti. High-Field Study of Muonium States in HfO_2 and ZrO_2. *Journal of Physics: Conference Series*, 551(1):012048, 2014.